materials

MDPI

Article

Influence of Nd Substitution on the Phase Constitution in (Zr,Ce)$Fe_{10}Si_2$ Alloys with the $ThMn_{12}$ Structure

Mieszko Kołodziej [1,2,*], Jean-Marc Grenèche [3], Sandy Auguste [3], Bogdan Idzikowski [1], Maciej Zubko [4,5], Lotfi Bessais [6] and Zbigniew Śniadecki [1]

1 Institute of Molecular Physics, Polish Academy of Sciences, Mariana Smoluchowskiego 17, 60-179 Poznań, Poland
2 NanoBioMedical Centre, Adam Mickiewicz University, Wszechnicy Piastowskiej 3, 61-614 Poznań, Poland
3 Institut des Molécules et Matériaux du Mans (IMMM, UMR CNRS 6283), Le Mans University, Avenue Olivier Messiaen, CEDEX 09, 72085 Le Mans, France
4 Institute of Materials Engineering, Faculty of Science and Technology, University of Silesia, 75 Pułku Piechoty 1a, 41-500 Chorzów, Poland
5 Department of Physics, Faculty of Science, University of Hradec Králové, Rokitanského 62, 500 03 Hradec Králové, Czech Republic
6 CNRS, ICMPE, University Paris Est Creteil, UMR 7182, 2 Rue Henri Dunant, 94320 Thiais, France
* Correspondence: kolodziej@ifmpan.poznan.pl

Abstract: Iron-based compounds with a $ThMn_{12}$-type structure have the potential to bridge the gap between ferrites and high performance $Nd_2Fe_{14}B$ magnets. From the point of view of possible applications, the main advantage is their composition, with about 10 wt.% less rare earth elements in comparison with the 2:14:1 phase. On the other hand, the main issue delaying the development of Fe-rich alloys with a $ThMn_{12}$-type structure is their structural stability. Therefore, various synthesis methods and stabilizing elements have been proposed to stabilize the structure. In this work, the influence of increasing Nd substitution on the phase constitution of $Zr_{0.4-x}Nd_xCe_{0.6}Fe_{10}Si_2$ ($0 \leq x \leq 0.3$) alloys was analyzed. X-ray diffraction and ^{57}Fe Mössbauer spectrometry were used as the main methods to derive the stability range and destabilization routes of the 1:12 structure. For the arc-melted samples, an increase in the lattice parameters of the $ThMn_{12}$-type structure was observed with the simultaneous growth of bcc-(Fe,Si) content with increasing Nd substitution. After isothermal annealing, the $ThMn_{12}$-type structure (and the coexisting bcc-(Fe,Si)) were stable over the whole composition range. While the formation of a 1:12 phase was totally suppressed in the as-cast state for x = 0.3, further heat treatment resulted in the growth of about 45% of the $ThMn_{12}$-type phase. The results confirmed that the stability range of $ThMn_{12}$-type structure in the Nd-containing alloys was well improved by other substitutions and the heat treatment, which in turn, is also needed to homogenize the $ThMn_{12}$-type phase. After further characterization of the magnetic properties and optimization of microstructure, such hard/soft magnetic composites can show their potential by exploiting the exchange spring mechanism.

Keywords: $ThMn_{12}$-type phase; permanent magnet; Mössbauer spectrometry; crystalline structure

Citation: Kołodziej, M.; Grenèche, J.-M.; Auguste, S.; Idzikowski, B.; Zubko, M.; Bessais, L.; Śniadecki, Z. Influence of Nd Substitution on the Phase Constitution in (Zr,Ce)$Fe_{10}Si_2$ Alloys with the $ThMn_{12}$ Structure. *Materials* **2023**, *16*, 1522. https://doi.org/10.3390/ma16041522

Academic Editor: Piotr Gębara

Received: 11 January 2023
Revised: 6 February 2023
Accepted: 9 February 2023
Published: 11 February 2023

1. Introduction

Currently, permanent magnets are widely used and the most known among them, with the highest energy product $BH_{|max|}$, are based on rare earth elements (REE), such as Sm or Nd [1,2], with well-known representatives in $Nd_2Fe_{14}B$ [3], Sm_2Co_{17} [4], and $Sm_2Fe_{17}N_3$ [5]. The range of possible applications is broad and is still growing [6]. With the development of new phases and the improvement of intrinsic and extrinsic properties, permanent magnets are still implemented in a rather trivial way, as a replacement of electromagnets, in loudspeakers and actuators, but also find more sophisticated applications in magnetic resonance imaging, in information storage devices, magnetic levitation, as

bearings, or as miniaturized magnetic field sensors [6,7]. The demand is still growing, as huge quantities of permanent magnets are used in, e.g., the automotive industry or wind turbine production [8]. Their criticality (growing demand with unstable supply chains) has led to the extensive research of new materials [9], where two important directions can be distinguished: (i) the decrease of REE content with preservation of magnets' magnetic performance and (ii) the search for novel REE-free hard magnetic materials, e.g., $L1_0$-FeNi [10] known from meteorites [11]. Moreover, there is a renewed interest in the tetragonal $ThMn_{12}$-type (1:12 stoichiometry) phase, which has already been known for decades [12]. This tetragonal structure is related to that of $SmCo_5$ of $CaCu_5$-type, where half of the rare earth atoms are replaced with transition metal dumbbells [7]. Even if its $BH_{|max|}$ would be slightly lower compared with high performance magnets, it would be still placed in the performance gap between cheaper ferrite-based and more expensive Nd-based magnets with 2:14:1 structure [13]. Nevertheless, another issue that has to be solved with these compounds is their structural stability. For most Fe- and REE-based compounds, $ThMn_{12}$-type phase is less stable than, for example, the hexagonal 2:17-type structure [14]. Therefore, stabilizing elements, such as Ti, V, Si or Al, have to be used [15–17]. For example, the $SmFe_{12}$ compound forms as a thin film, but is unstable in bulk [18]. In such cases, large transition metal atoms are needed to stabilize the structure, as in $SmFe_{11}Ti$ [19]. The simultaneous substitution of other elements, for example, Zr on rare earth sites and Co on Fe sites, allowed a decrease in Ti content in $(Sm_{0.8}Zr_{0.2})$ $(Fe_{0.75}Co_{0.25})_{11.5}Ti_{0.5}$ and the optimization of the magnetic properties [20]. Additionally, there are several further issues that must be taken into account, such as microstructure and twinning [18,21]. One of the largest groups of alloys with the $ThMn_{12}$ structure is based on Sm [22–25]. Nonetheless, for already known and investigated 1:12-type compounds, the maximum effort was made to develop Ce-based compounds due to the low criticality of this element [26–28]. Recently, the formation of the $ThMn_{12}$ structure (almost 100% of volume fraction) has been confirmed in $Zr_{0.4}Ce_{0.6}Fe_{10}Si_2$ [29]. The Ce substitution increased the anisotropy field from 16.9 kOe for $ZrFe_{10}Si_2$ to 24 kOe for $Zr_{0.4}Ce_{0.6}Fe_{10}Si_2$. Replacement of Zr by Nd in $ZrFe_{10}Si_2$ and further nitrogenation of this alloy have also been investigated [30] and are believed to be very promising in the optimization of hard magnetic properties. $Nd_{0.4}Zr_{0.6}Fe_{10}$-Si_2 has been also examined to confirm whether the formation of the $ThMn_{12}$-type phase is possible and to determine its magnetic and structural properties [31]. It has also been shown than the replacement of Fe atoms by Co improved magnetic performance, with the enhancement of the Curie temperature as a main benefit [31]. These results raised a question: how would substitution of Zr by Nd in $Zr_{0.4}Ce_{0.6}Fe_{10}Si_2$ affect formation of the 1:12 structure [29]? Nd is believed to enhance the magnetic performance of this alloy [32]. As-cast samples were also isothermally annealed at 1373 K, the temperature which has been reported before [33], to lie in the stability region for $ThMn_{12}$ phase formation. Therefore, on the basis of structural and spectroscopic measurements, the structural stability of the $ThMn_{12}$-type phase in the Nd-substituted $Zr_{0.4}Ce_{0.6}Fe_{10}Si_2$ alloy was determined in this paper.

2. Methods

Samples with $Zr_{0.4-x}Nd_xCe_{0.6}Fe_{10}Si_2$ ($0 \leq x \leq 0.3$) compositions were prepared by arc-melting in an argon atmosphere. The melting procedure was repeated several times to ensure homogeneity. Additionally, residual oxygen was gathered by melting a Zr getter. Afterwards, samples wrapped in Ta foil were placed in quartz capsules, which were then evacuated three times with the use of turbomolecular pump (down to 10^{-4} mbar), refilled with Ar up to 500 mbar and sealed. Samples were then annealed isothermally at 1373 K in the Carbolite MTF 12/25/250 tube furnace for 72 h and subsequently quenched in cold water. For microscopic measurements, the powdered sample was suspended in isopropyl alcohol, and the resulting material, after dispersion in an ultrasonic bath for 30 min, was deposited on a Cu grid with an amorphous carbon film standardized for transmission electron microscope (TEM) observations. Structural analysis was performed

using X-ray powder diffraction (XRPD). Patterns were recorded with a PANalytical X'Pert Pro diffractometer in Bragg–Brentano geometry (CoK_α radiation). A cobalt anode was chosen to avoid X-ray fluorescence of iron compounds. Data were collected in the range of 2θ from 20 to 110° with a 0.0167° step and 400 s per step for a total acquisition time of 5 h. X-ray diffraction patterns were analyzed using MAUD software (Rietveld method combined with Fourier analysis) [34] to determine the phase constitution, volume fractions and lattice parameters of various phases. Transmission ^{57}Fe Mössbauer effect experiments were performed at room temperature (RT) using a constant acceleration conventional spectrometer with a ^{57}Co source. Samples were powdered using an Fe-free tool. The powder obtained was collected and placed in an altuglass sample holder with a content of about 5 mg Fe/cm^2. The hyperfine structure was modeled by least square refinement involving magnetic and quadrupolar components with Lorentzian lines. The values of the isomer shift are quoted relative to those of bcc-Fe at RT. Initial measurements were made in the range from −12 to 12 mm/s, to check the presence of oxides. Final spectra with improved statistics were measured from −8 to 8 mm/s. Microstructure analysis of the selected samples was carried out using JEOL JEM-3010 high-resolution transmission electron microscope with 300 kV acceleration voltage, equipped with a Gatan 2k × 2k Orius™ 833 SC200D CCD camera. Recorded selected area electron diffraction (SAED) patterns, as well as the calculated Fast Fourier Transforms (FFT) from high-resolution images were indexed using ElDyf [35] computer software.

3. Results and Discussion

The X-ray diffraction patterns for $Zr_{0.4-x}Nd_xCe_{0.6}Fe_{10}Si_2$ ($0 \leq x \leq 0.3$) alloys synthesized by the arc-melting method are shown in Figure 1. The $Zr_{0.4}Ce_{0.6}Fe_{10}Si_2$ alloy contains about 90% of the $ThMn_{12}$-type structure with the addition of about 10% of bcc-(Fe,Si) phase. The presence of Si in bcc structure was expected, taking into account changed lattice parameter values (Table 1), and was confirmed by spectroscopic measurements. By replacing 25 at.%, 50 at.% and 75 at.% of Zr by Nd, we obtained nominally $Zr_{0.3}Nd_{0.1}Ce_{0.6}Fe_{10}Si_2$, $Zr_{0.2}Nd_{0.2}Ce_{0.6}Fe_{10}Si_2$, and $Zr_{0.1}Nd_{0.3}Ce_{0.6}Fe_{10}Si_2$ alloys. In the first case, about 82% of the $ThMn_{12}$-type structure and 18% of bcc-(Fe,Si) phase formed. Substitution of 50% of Zr by Nd led to further suppression of $ThMn_{12}$-type phase formation and facilitated the growth of highly disordered hexagonal phase, nominally (REE)Fe_5. About 52% of $ThMn_{12}$-type phase formed along with 25% of the bcc-(Fe,Si) phase and an insignificant amount of α-Zr. One must bear in mind that the fitting procedure for an α-Zr phase is based just on two reflections. Therefore, this finding should be treated with a caution. Nevertheless, for clarity reasons, we use this designation throughout the paper. In $Zr_{0.1}Nd_{0.3}Ce_{0.6}Fe_{10}Si_2$, the $ThMn_{12}$-type structure was not observed, while the presence of hexagonal-type phase, bcc-(Fe,Si) phase and α-Zr was confirmed. The bcc-(Fe,Si) lattice parameter does not vary much depending on the Nd content, and the bcc lattice contained about 8–10 at.% of Si in every investigated sample. The Nd influence on the values of $ThMn_{12}$-type phase lattice parameters and lattice volume was noticed, where all parameters (a = b and c) increased with the growth of Nd content (Table 1). Along with the influence of thermodynamic parameters (e.g., enthalpies of formation), lattice expansion could be one of the main reasons for the instability of the $ThMn_{12}$-type structure for large substitutions of Zr by Nd. Detailed results are presented in Figure 2. Zirconium and silicon play a significant role in the stabilization of the $ThMn_{12}$-type structure in Fe-based alloys [29,30]. The influence of Nd, Ce and Zr on the enthalpies of formation of various phases in the Fe-Si-based alloys has been also analyzed by us lately [36]. Beneficial influence of Zr on the formation of the $ThMn_{12}$-type phase was confirmed, but the enthalpy of formation of other competing phases (i.e., bcc solid solution and amorphous phase) also decreased significantly with increased Zr content. When we analyzed enthalpy values only, it has been reported that Ce and Nd should have deteriorating impact on the stability of crystalline phases. Nevertheless, with small rare earth element substitutions, other quantities such as a mismatch entropy [36] or site preference [30] play a role in the formation of $ThMn_{12}$-type phase.

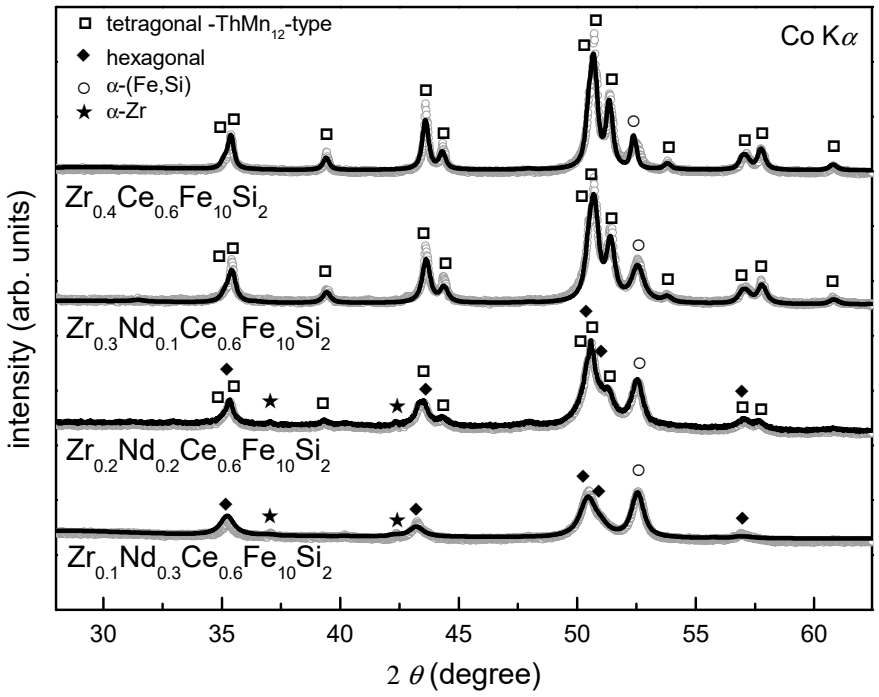

Figure 1. X-ray diffraction patterns of arc-melted $Zr_{0.4-x}Nd_xCe_{0.6}Fe_{10}Si_2$ ($0 \leq x \leq 0.3$) alloys. $ThMn_{12}$-type structure, α-(Fe,Si), α-Zr and highly disordered hexagonal structure were identified and marked with respective symbols.

Table 1. Refined values of the lattice parameters of the two phases identified for $Zr_{0.4-x}Nd_xCe_{0.6}Fe_{10}Si_2$ ($0 \leq x \leq 0.3$) samples after arc-melting and annealing at 1373 K for 72 h: bcc-(Fe,Si) and $ThMn_{12}$-type structure.

Nd Content		x = 0	x = 0	x = 0.1	x = 0.1	x = 0.2	x = 0.2	x = 0.3	x = 0.3
Phase	**Lattice Parameter**	**Arc-Melted**	**Annealed**	**Arc-Melted**	**Annealed**	**Arc-Melted**	**Annealed**	**Arc-Melted**	**Annealed**
bcc-(Fe,Si)	a = b = c [±0.001]	2.862	2.863	2.862	2.863	2.860	2.861	2.864	2.861
$ThMn_{12}$	a = b [±0.001]	8.389	8.385	8.401	8.404	8.405	8.415	-	8.428
	c [±0.001]	4.744	4.736	4.745	4.741	4.752	4.742	-	4.750

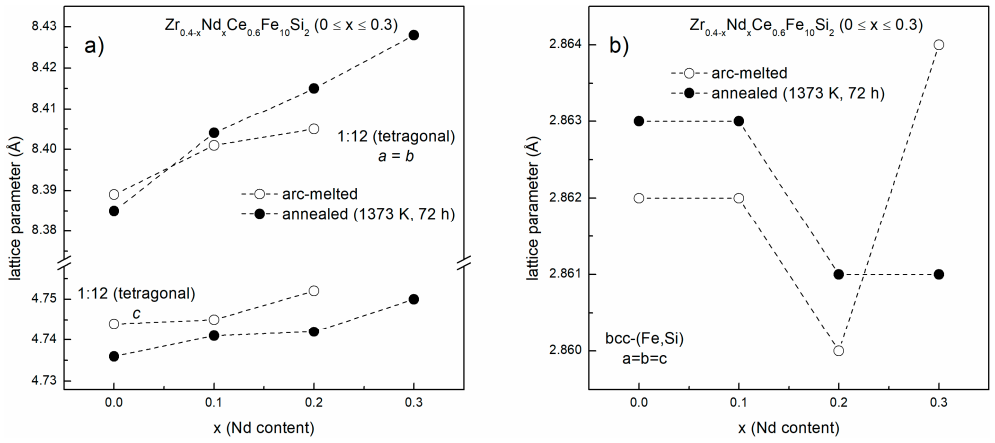

Figure 2. Refined values of lattice parameters for (**a**) $ThMn_{12}$ and (**b**) bcc-(Fe,Si) structures according to Nd content for arc-melted (white points) and annealed at 1373 K for 72 h (black points) $Zr_{0.4-x}Nd_xCe_{0.6}Fe_{10}Si_2$ ($0 \leq x \leq 0.3$) alloys.

Mössbauer spectrometry was used to support the structural investigations. Several sextets with different hyperfine field parameters, suggesting a multiphase character of investigated samples and numerous magnetically distinguishable surroundings of Fe atoms were observed. As already mentioned, the spectrum initially assigned in the fitting procedure to be bcc-Fe was non-typical, as it was composed of at least three sub-spectra. The determined hyperfine parameters values were confronted with the literature data [37]. We considered the values of specific hyperfine field parameters and applied them in a fitting model according to wt.% of Si in Fe [37]. The results suggested, along with the lattice parameter value of bcc phase, that the observed bcc-Fe phase was in fact the bcc-(Fe,Si). Part of Si diffuses into the bcc lattice and is not directly involved in the $ThMn_{12}$-type structure stabilization. Mössbauer spectra are shown in Figure 3, while hyperfine parameters are listed in Table 2. Notably, more precise estimation of Si content in bcc lattice was possible, as the lattice parameter of bcc structure and Si content were linearly dependent on each other [38]. Therefore, it was possible to extrapolate refined lattice parameter to confirm the content of Si diffusing into the bcc structure.

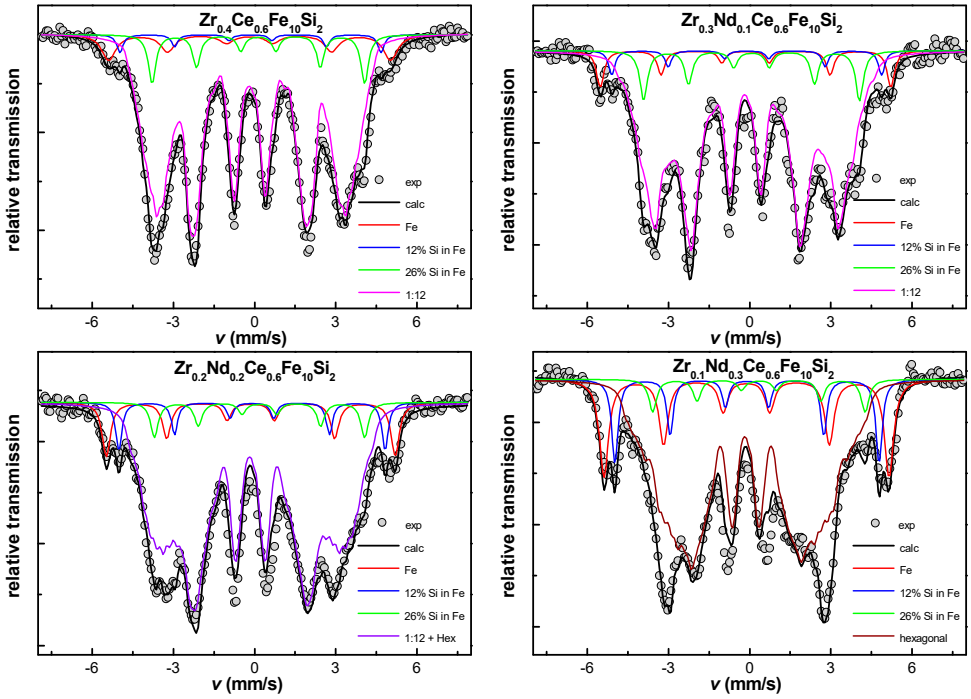

Figure 3. Mössbauer spectra in arc-melted $Zr_{0.4-x}Nd_xCe_{0.6}Fe_{10}Si_2$ ($0 \leq x \leq 0.3$) alloys.

Afterwards, isothermal annealing of arc-melted alloys at 1373 K for 72 h (conditions favorable for $ThMn_{12}$-type structure formation [33]) was performed. X-ray diffraction patterns are shown in Figure 4. After heat treatment, higher precipitation of bcc-(Fe,Si) was observed for the parent $Zr_{0.4}Ce_{0.6}Fe_{10}Si_2$ alloy, with about 17% of total volume fraction, when compared to 10% in the arc-melted sample. A small amount of 2:17 structure formation and an insignificant amount of $ZrFeSi_2$ phase were also noticed. In contrast to as-cast samples, the $ThMn_{12}$-type phase was present in the whole composition range in the annealed samples. As observed in arc-melted samples already, Nd-substitution led to a decreasing volume fraction of the $ThMn_{12}$-type structure. The inverse dependence was observed for the bcc-(Fe,Si) phase. The amount of hexagonal 2:17-type phase and $ZrFeSi_2$ phase did not exceed 5 at.% in the whole composition range. Silicon content in the bcc lattice was determined by estimating the lattice parameter [37,38]. Its content is in the range of 9–10 at.%, in accordance with the previous results for the as-cast samples. Lattice parameters of $ThMn_{12}$-type phase increased with Nd content (Table 1). As the refinement of the lattice parameters was made using the Rietveld method, the estimated standard

deviation was the only measure of the uncertainty of the lattice parameters which did not exceed 0.001 Å.

Table 2. Refined values of the hyperfine parameters of the phases identified for arc-melted $Zr_{0.4-x}Nd_xCe_{0.6}Fe_{10}Si_2$ ($0 \leq x \leq 0.3$) samples.

Phase		B_{hf} (T) [±0.5]	δ (mm/s) [±0.01]	2ε (mm/s) [±0.01]	Area % [±2]
$Zr_{0.4}Ce_{0.6}Fe_{10}Si_2$					
$ThMn_{12}$		<28.7>	<−0.13>	<0.06>	88
bcc-(Fe,Si)	bcc-Fe	32.3	−0.17	0	3
	Fe—12% Si	30.4	−0.1	0	2
	Fe—26% Si	24.5	−0.1	0	7
$Zr_{0.3}Nd_{0.1}Ce_{0.6}Fe_{10}Si_2$					
$ThMn_{12}$		<28.7>	<0.05>	<0.05>	83
bcc-(Fe,Si)	bcc-Fe	33.1	−0.15	0	6
	Fe—12% Si	30.8	−0.11	0	3
	Fe—26% Si	24.6	0.07	0	8
$Zr_{0.2}Nd_{0.2}Ce_{0.6}Fe_{10}Si_2$					
$ThMn_{12}$ + hex		<29.9>	<−0.14>	<0.0>	76
bcc-(Fe,Si)	bcc-Fe	32.8	−0.14	0	11
	Fe—12% Si	30.3	−0.09	0	7
	Fe—26% Si	24.1	0.18	0	6
$Zr_{0.1}Nd_{0.3}Ce_{0.6}Fe_{10}Si_2$					
Nd(Zr, Ce)Fe hex		<30.6>	<−0.14>	<0.02>	66
bcc-(Fe,Si)	bcc-Fe	32.6	−0.12	0	17
	Fe—12% Si	30.1	−0.1	0	11
	Fe—26% Si	24.2	0.3	0	6

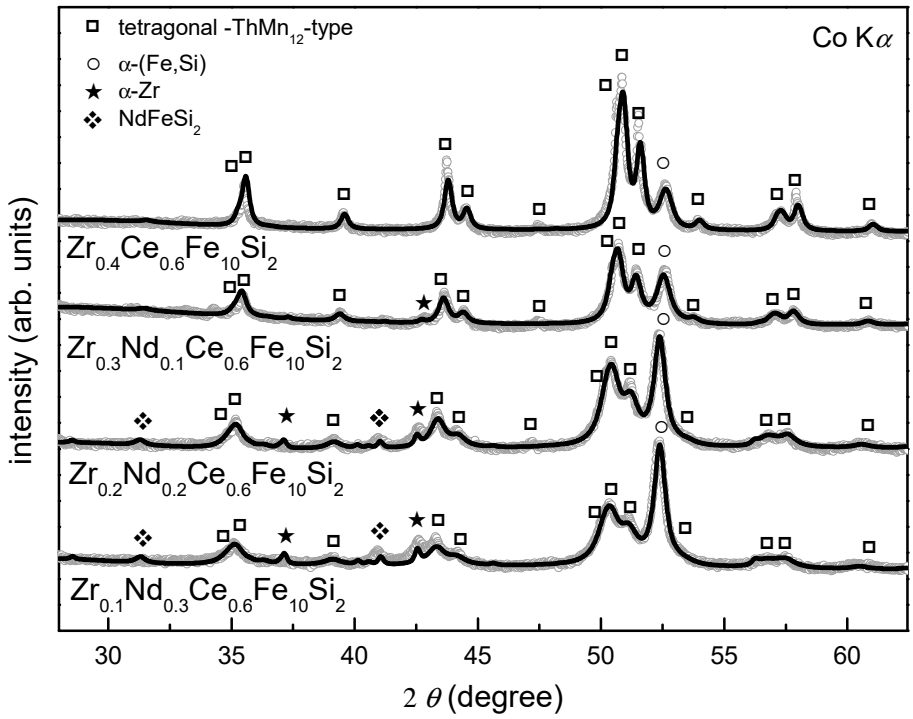

Figure 4. X-ray diffraction patterns of $Zr_{0.4-x}Nd_xCe_{0.6}Fe_{10}Si_2$ ($0 \leq x \leq 0.3$) alloys annealed at 1373 K for 72 h, mainly composed of $ThMn_{12}$-type structure.

The Mössbauer spectrometry results showed that the $ThMn_{12}$-type structure obtained after arc-melting was clearly not homogeneous. As it was not possible to describe three subspectra for 8i, 8j and 8f positions (Figure 3), a distribution of parameters was used by similarity to these already known from previous investigations, where Ce substitution for Nd in similar alloys was reported to be responsible for lowering of the hyperfine field (B_{hf}) [39–41]. Consequently, the mean value of the hyperfine field parameter was checked and estimated to be equal to 28.7 ± 0.5, 28.7 ± 0.5, 29.9 ± 0.5 and 30.6 ± 0.5 T for the $Zr_{0.4}Ce_{0.6}Fe_{10}Si_2$, $Zr_{0.3}Nd_{0.1}Ce_{0.6}Fe_{10}Si_2$, $Zr_{0.2}Nd_{0.2}Ce_{0.6}Fe_{10}Si_2$, and $Zr_{0.1}Nd_{0.3}Ce_{0.6}Fe_{10}Si_2$, respectively. This slight increase was connected with the growth of a disordered hexagonal phase replacing the $ThMn_{12}$-type one. All hyperfine parameters determined from the spectra shown in Figure 3 are presented in Table 2. We observed the evolution of spectra with Nd substitution, which is in accordance with X-ray diffraction results, and we concluded that the content of pure bcc-Fe phase (with no Si in the nearest neighborhood) increases from 3% for $Zr_{0.4}Ce_{0.6}Fe_{10}Si_2$, to 6, 11 and 17% for $Zr_{0.3}Nd_{0.1}Ce_{0.6}Fe_{10}Si_2$, $Zr_{0.2}Nd_{0.2}Ce_{0.6}Fe_{10}Si_2$, and $Zr_{0.1}Nd_{0.3}Ce_{0.6}Fe_{10}Si_2$, respectively. The same trend occurred for the bcc phase sub spectrum that was assumed to contain 12 at.% of Si (from 2, through 3, 7 up to 11% with increasing Nd content). The content of another sub-spectrum (bcc phase with 26 at.% of Si in Fe) is equal to about 6% for each sample. Small inaccuracies are possible because of overlapping spectra with hyperfine field parameters of about 24 T, coming from both the $ThMn_{12}$-type structure and bcc phase with 26 at.% of Si in Fe. Annealed samples revealed much better homogeneity than arc-melted alloys, as shown by more consistent positions and narrower peaks observed in Mössbauer spectra (Figure 5). The spectra for 8i, 8j and 8f positions for the $ThMn_{12}$-type phase were fully described. The hyperfine field parameter of Fe in 8i and 8j positions increased with the substitution of Nd for Zr (Table 3). Variation of B_{hf} was not so evident for the 8f position. It changed from 19.8 ± 0.5, through 19.4 ± 0.5, 19.5 ± 0.5 to 19.4 ± 0.5 T with the increasing Nd content. There is also a doublet visible in the middle of the Mössbauer spectra of all annealed samples, whose contribution increased with Nd substitution. It was assumed to originate from (Zr,Nd,Ce)$FeSi_2$ phase, as its content also follows the annealed alloys' constitution determined on the basis of X-ray diffraction. One must bear in mind the presence of grain boundaries (GB), which may play a large role while analyzing the Mössbauer spectra. Their contribution was estimated to be equal to about 10%, with a B_{hf} mean value varying from 19.8 ± 0.5 T for $Zr_{0.4}Ce_{0.6}Fe_{10}Si_2$, through 18.7 ± 0.5, 18.3 ± 0.5, down to 18.2 ± 0.5 T, for $Zr_{0.3}Nd_{0.1}Ce_{0.6}Fe_{10}Si_2$, $Zr_{0.2}Nd_{0.2}Ce_{0.6}Fe_{10}Si_2$, and $Zr_{0.1}Nd_{0.3}Ce_{0.6}Fe_{10}Si_2$, respectively. Their presence can have a great influence on the magnetic properties of nanocomposite [40,41].

To examine the microstructure of the samples obtained and to confirm the phase composition obtained by X-ray diffraction, transmission electron microscopy (TEM) was performed on two selected samples: arc melted and annealed $Zr_{0.4}Ce_{0.6}Fe_{10}Si_2$. The TEM measurements were performed mainly to confirm the existence of grain boundaries, which were presumed mainly on the basis of Mössbauer spectrometry results. We took advantage of the use of this method to confirm simultaneously that, in fact, we deal mainly with $ThMn_{12}$-type and (Fe,Si)-bcc phases. Nevertheless, we observed that the phase constitution and the mean crystallite size differ for various pieces of the same sample. Therefore, we omitted a more detailed analysis as it would not bring the results, which are representative for the sample as a whole. Nonetheless, the sample after arc-melting showed coarse grains. Electron diffraction measurements confirmed the presence of the tetragonal $ThMn_{12}$-type structure and the bcc-(Fe,Si) phase (Figure 6). TEM observations of the annealed sample were in good agreement with the X-ray diffraction results. The tetragonal $ThMn_{12}$-type phase and bcc-(Fe,Si) phase were also observed in the annealed sample. It was not able to determine the crystallite sizes of $ThMn_{12}$-type phase precisely. For the bcc-(Fe,Si) phase, the recorded high-resolution images revealed a well-crystallized nanocrystalline structure with a crystallite size of about 9 nm (Figure 7). Some grain boundaries and/or structurally disordered regions are also visible, as suggested before by Mössbauer spectrometry.

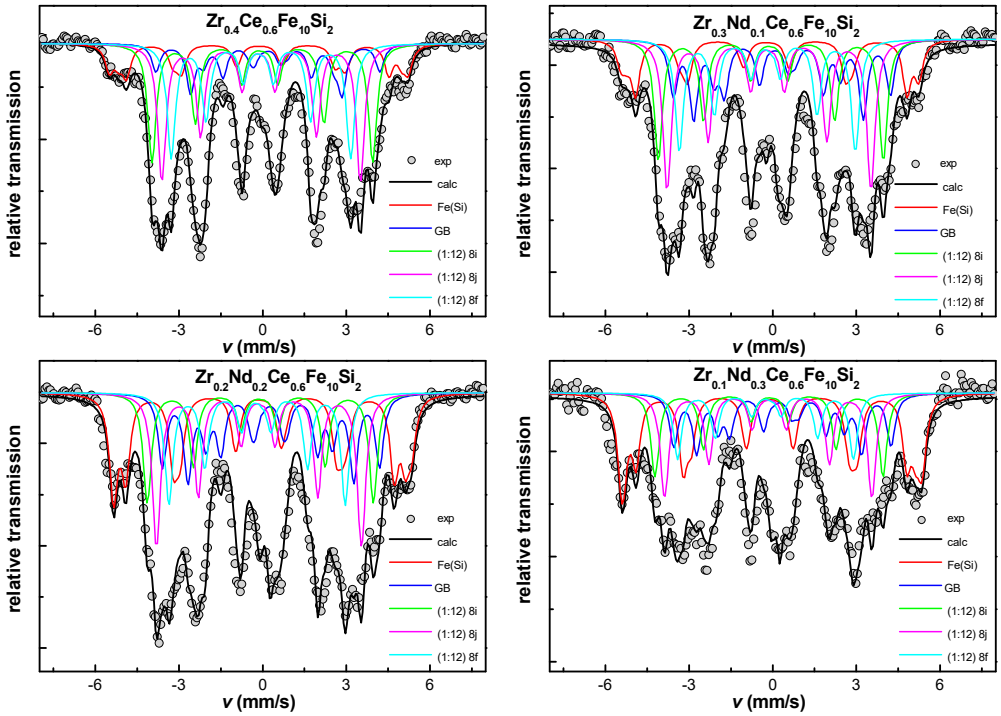

Figure 5. Mössbauer spectra of $Zr_{0.4-x}Nd_xCe_{0.6}Fe_{10}Si_2$ ($0 \leq x \leq 0.3$) alloys annealed at 1373 K for 72 h.

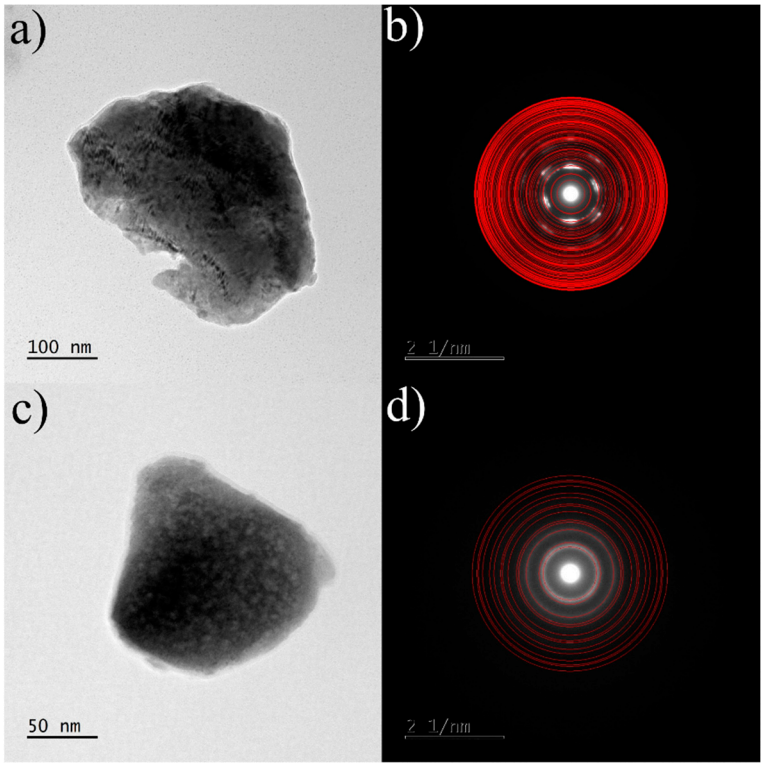

Figure 6. TEM images of the arc melted $Zr_{0.4}Ce_{0.6}Fe_{10}Si_2$ sample: (**a**) bright field image of the particle with predominantly $ThMn_{12}$-type phase with (**b**) corresponding selected area electron diffraction pattern and (**c**) bright field image of the particle with predominantly bcc-(Fe,Si)-like phase with (**d**) corresponding selected area electron diffraction pattern. Red rings on the SAED patterns indicate theoretical Bragg positions for both phases.

Table 3. Refined values of the hyperfine parameters of the two phases (bcc-(Fe,Si) and $ThMn_{12}$-type structure) identified for $Zr_{0.4-x}Nd_xCe_{0.6}Fe_{10}Si_2$ ($0 \leq x \leq 0.3$) samples annealed at 1373 K for 72 h.

Phase		B_{hf} (T) [±0.5]	δ (mm/s) [±0.01]	2ε (mm/s) [±0.01]	Area % [±2]
$Zr_{0.4}Ce_{0.6}Fe_{10}Si_2$					
$ThMn_{12}$	8i	24.4	−0.06	0.09	23
	8j	21.9	−0.1	0.09	26
	8f	19.8	−0.1	0.09	22
bcc-(Fe,Si)	bcc-Fe	33.1	−0.12	−0.03	5
	Fe—4.5% Si	31.3	−0.08	−0.03	3
	Fe—12% Si	29.1	−0.16	−0.03	6
	Fe—26% Si	24.7	0.2	−0.03	5
$Zr_{0.3}Nd_{0.1}Ce_{0.6}Fe_{10}Si_2$					
$ThMn_{12}$	8i	24.9	−0.1	0.06	20
	8j	22.5	−0.16	0.06	24
	8f	19.4	−0.22	0.06	18
bcc-(Fe,Si)	bcc-Fe	33	−0.18	0.17	4
	Fe—4.5% Si	32.3	−0.08	0.17	2
	Fe—12% Si	30	−0.13	0.17	9
	Fe—26% Si	24	0.25	0.17	9
$Zr_{0.2}Nd_{0.2}Ce_{0.6}Fe_{10}Si_2$					
$ThMn_{12}$	8i	25	−0.1	0.04	15
	8j	22.7	−0.15	0.04	21
	8f	19.5	−0.21	0.04	15
bcc-(Fe,Si)	bcc-Fe	33	−0.03	0.06	6
	Fe—4.5% Si	32.3	−0.15	0.06	8
	Fe—12% Si	29.7	−0.12	0.06	10
	Fe—26% Si	24	0.27	0.06	10
$Zr_{0.1}Nd_{0.3}Ce_{0.6}Fe_{10}Si_2$					
$ThMn_{12}$	8i	25.2	−0.12	−0.03	15
	8j	22.9	−0.14	−0.03	18
	8f	19.4	−0.24	−0.03	12
bcc-(Fe,Si)	bcc-Fe	33.3	−0.06	−0.03	12
	Fe—4.5% Si	32.3	−0.13	−0.03	7
	Fe—12% Si	30	−0.07	−0.03	12
	Fe—26% Si	24	0.32	−0.03	9

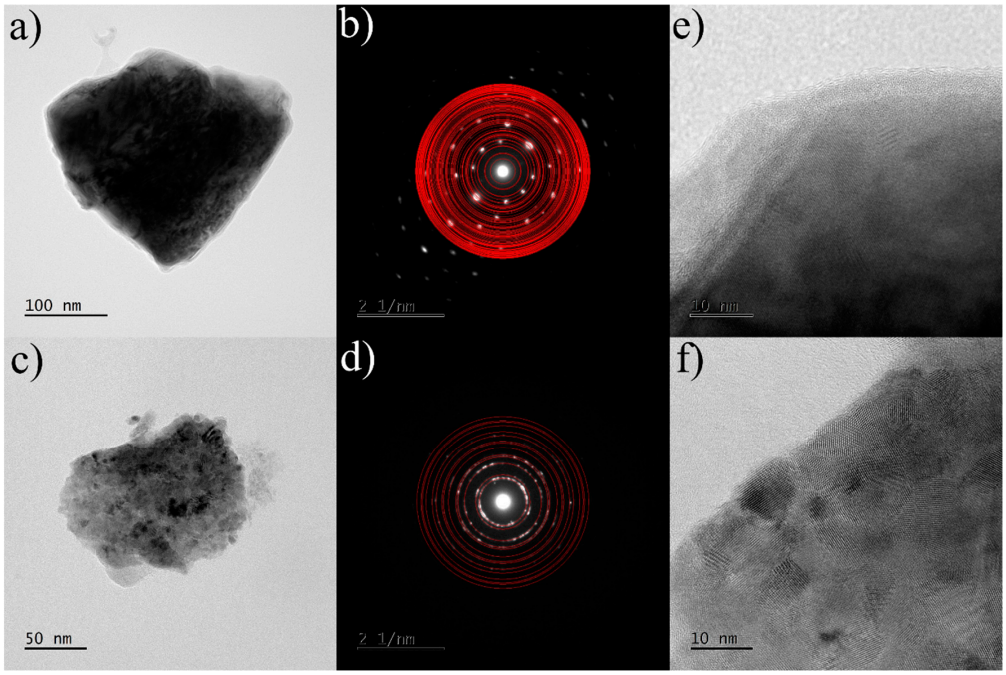

Figure 7. TEM images of the $Zr_{0.4}Ce_{0.6}Fe_{10}Si_2$ sample annealed at 1373 K for 72 h: (**a**) bright field image of the particle with predominantly $ThMn_{12}$-type phase with (**b**) corresponding selected area electron diffraction pattern and (**c**) bright field image of the particle with predominantly bcc-(Fe,Si)-like phase with (**d**) corresponding selected area electron diffraction pattern. High-resolution images of the $ThMn_{12}$-like phase and bcc-(Fe,Si)-like phase are shown in (**e**,**f**), respectively. Red rings on the SAED patterns indicate theoretical Bragg positions for both phases.

4. Conclusions

Several $Zr_{0.4-x}Nd_xCe_{0.6}Fe_{10}Si_2$ ($0 \leq x \leq 0.3$) alloys mainly composed of a $ThMn_{12}$-type structure were synthesized by arc-melting and subsequent annealing. The presence of the bcc phase, which was found to contain Si with a rather stable content throughout the whole series of samples (about 9–10 at.% of Si in bcc-Fe lattice), was confirmed for all samples. Moreover, a facilitated formation of bcc-(Fe,Si) was observed with increasing Nd content. The $ThMn_{12}$-type structure became less stable with increasing Nd content, also due to a slight increase in lattice parameters/volume. The ^{57}Fe Mössbauer spectrometry results confirmed that the $ThMn_{12}$-type structure in the pre-annealed samples was highly disordered, and that the distribution of hyperfine parameters had to be used to describe the spectra correctly. For an equiatomic Zr/Nd composition, the crystallization of a highly disordered hexagonal phase, nominally $(REE)Fe_5$, was observed. This process resulted in a simultaneous decrease in the driving force for the formation of a $ThMn_{12}$-type structure (totally suppressed for x = 0.3). In contrast, the $ThMn_{12}$-type phase was present in the whole composition range, along with the bcc-(Fe,Si), in the annealed samples. In addition, the growth of the 2:17 hexagonal phase was observed, whose content increased with Nd substitution (from 2 at.% up to 5 at.%). Importantly, the $ThMn_{12}$ structure became more homogeneous after annealing. The homogeneity, as well as the improved stability, of the $ThMn_{12}$-type phase (even for high Nd substitution) confirms that the preconceived synthesis route and the choice of stabilizing elements (Si, Zr, Nd, Ce) were appropriate for the future development of these alloys. It was evident that Nd adversely affected stability of 1:12 structure, but it was confirmed that the preservation of its high content was still possible (with Zr, Ce and Si substitution). Further experiments are needed to determine the influence of Nd-substitution on magnetic properties. Moreover, attention should be drawn to the possibilities of exploitation of the exchange spring effect, due to the presence of a soft magnetic bcc phase. By optimizing the content of hard and soft magnetic phases

and their microstructure [42], one can expect improved values of coercivity and remanent magnetization, leading to the maximization of overall magnet performance.

Author Contributions: Conceptualization, M.K. and Z.Ś.; Data curation, M.K., J.-M.G., M.Z. and Z.Ś.; Formal analysis, M.K., J.-M.G. and Z.Ś.; Investigation, M.K., S.A., J.-M.G. and M.Z.; Methodology, M.K., J.-M.G. and Z.Ś.; Supervision, Z.Ś.; Validation, M.K. and Z.Ś.; Visualization, M.K., M.Z. and Z.Ś.; Writing—Original draft, M.K. and M.Z., Writing—review & editing, M.K., J.-M.G., S.A., B.I., L.B. and Z.Ś. All authors have read and agreed to the published version of the manuscript.

Funding: M.K. was financially supported by the project "Środowiskowe interdyscyplinarne studia doktoranckie w zakresie nanotechnologii" ("Environmental interdisciplinary doctoral studies in nanotechnology") No. POWR.03.02.00-00-I032/16 under the European Social Fund –Operational Programme Knowledge Education Development, Axis III Higher Education for Economy and Development, Action 3.2 PhD Programme. Financial support of B.I. investigations by the Polish Academy of Sciences in the framework of the Polish-French cooperation between PAS and CNRS in the form of long-term visit is also acknowledged.

Institutional Review Board Statement: Not applicable.

Informed Consent Statement: Not applicable.

Data Availability Statement: The data presented in this study are available on request from the corresponding author.

Acknowledgments: The authors thank Agnieszka Grabias for discussions and critical revision.

Conflicts of Interest: The authors declare no conflict of interest.

References

1. Pflüger, J.; Heinen, W.; Gudat, W. On the thermal stability of the $SmCo_5$ magnet structure for the BESSY undulator. *Nucl. Instrum. Methods Phys. Res. Sect. B Accel. Spectrom. Detect. Assoc. Equip.* **1987**, *262*, 528–533. [CrossRef]
2. Sagawa, M.; Fujimura, S.; Togawa, N.; Yamamoto, H.; Matsuura, Y. New material for permanent magnets on a base of Nd and Fe (invited). *J. Appl. Phys.* **1984**, *55*, 2083–2087. [CrossRef]
3. Sagawa, M.; Fujimura, S.; Yamamoto, H.; Matsuura, Y.; Hiraga, K. Permanent magnet materials based on the rare earth-iron-boron tetragonal compounds. *IEEE Trans. Magn.* **1984**, *20*, 1584–1589. [CrossRef]
4. Kumar, K. $RETM_5$ and RE_2TM_{17} permanent magnets development. *J. Appl. Phys.* **1988**, *63*, R13–R57. [CrossRef]
5. Iriyama, T.; Kobayashi, K.; Imaoka, N.; Fukuda, T.; Kato, H.; Nakagawa, Y. Effect of nitrogen content on magnetic properties of $Sm_2Fe_{17}N_x$ ($0 < x < 6$). *IEEE Trans. Magn.* **1992**, *28*, 2326–2331. [CrossRef]
6. Coey, J.M.D. Permanent magnet applications. *J. Magn. Magn. Mater.* **2002**, *248*, 441–456. [CrossRef]
7. Hirosawa, S.; Nishino, M.; Miyashita, S. Perspectives for high-performance permanent magnets: Applications, coercivity, and new materials. *Adv. Nat. Sci. Nanosci. Nanotechnol.* **2017**, *8*, 013002. [CrossRef]
8. Takahashi, Y.; Sepehri-Amin, H.; Ohkubo, T. Recent advances in SmFe12-based permanent magnets. *Sci. Technol. Adv. Mater.* **2021**, *22*, 449–460. [CrossRef]
9. Skomski, R.; Manchanda, P.; Kumar, P.; Balasubramanian, B.; Kashyap, A.; Sellmyer, D. Predicting the Future of Permanent-Magnet Materials. *Trans. Magn.* **2013**, *49*, 3215. [CrossRef]
10. Paulevé, J.; Chamberod, A.; Krebs, K.; Bourret, A. Magnetization Curves of Fe–Ni (50–50) Single Crystals Ordered by Neutron Irradiation with an Applied Magnetic Field. *J. Appl. Phys.* **1968**, *39*, 989–990. [CrossRef]
11. Lewis, L.H.; Mubarok, A.; Poirier, E.; Bordeaux, N.; Manchanda, P.; Kashyap, A.; Skomski, R.; Goldstein, J.; Pinkerton, F.E.; Mishra, R.K. Inspired by nature: Investigating tetrataenite for permanent magnet applications. *J. Phys. Condens. Matter* **2014**, *26*, 064213. [CrossRef]
12. Solzi, M.; Pareti, L.; Moze, O.; David, W.I.F. Magnetic anisotropy and crystal structure of intermetallic compounds of the $ThMn_{12}$ structure. *J. Appl. Phys.* **1988**, *64*, 5084–5087. [CrossRef]
13. Coey, J.M.D. Permanent magnets: Plugging the gap. *Scr. Mater.* **2012**, *67*, 524–529. [CrossRef]
14. Harashima, Y.; Fukazawa, T.; Kino, H.; Miyake, T. Effect of R-site substitution and the pressure on stability of RFe_{12}: A first-principles study. *J. Appl. Phys.* **2018**, *124*, 163902. [CrossRef]
15. Schultz, L.; Schnitzke, K.; Wecker, J. High coercivity in mechanically alloyed Sm-Fe-V magnets with a $ThMn_{12}$ crystal structure. *Appl. Phys. Lett.* **1990**, *56*, 868–870. [CrossRef]
16. Buschow, K.H.J. Permanent magnet materials based on tetragonal rare earth compounds of the type $RFe_{12-x}M_x$. *J. Magn. Magn. Mater.* **1991**, *100*, 79–89. [CrossRef]
17. Fu, J.B.; Yu, X.; Qi, Z.Q.; Yang, W.Y.; Liu, S.Q.; Wang, C.S.; Du, H.L.; Han, J.Z.; Yang, Y.C.; Yang, J.B. Magnetic properties of $Nd(Fe_{1-x}Co_x)_{10.5}M_{1.5}$ (M = Mo and V) and their nitrides. *AIP Adv.* **2016**, *7*, 056202. [CrossRef]

18. Gabay, A.M.; Hadjipanayis, G.C. Recent developments in RFe_{12}-type compounds for permanent magnets. *Scr. Mater.* **2018**, *154*, 284–288. [CrossRef]
19. Isnard, O.; Guillot, M.; Miraglia, S.; Fruchart, D. High field magnetization measurements of $SmFe_{11}Ti$ and $SmFe_{11}TiH_{1-\delta}$. *J. Appl. Phys.* **1996**, *79*, 5542. [CrossRef]
20. Kuno, T.; Suzuki, S.; Urushibata, K.; Kobayashi, K.; Sakuma, N.; Yano, M.; Kato, A.; Manabe, A. $(Sm,Zr)(Fe,Co)_{11.0\text{-}11.5}Ti_{1.0\text{-}0.5}$ compounds as new permanent magnet materials. *AIP Adv.* **2016**, *6*, 025221. [CrossRef]
21. Ener, S.; Skokov, K.P.; Palanisamy, D.; Devillers, T.; Fischbacher, J.; Eslava, G.G.; Maccari, F.; Schäfer, L.; Diop, L.V.B.; Radulov, I.; et al. Twins—A weak link in the magnetic hardening of $ThMn_{12}$-type permanent magnets. *Acta Mater.* **2021**, *214*, 116968. [CrossRef]
22. Matsumoto, M.; Hawai, T.; Ono, K. $(Sm,Zr)Fe_{12-x}M_x$ (M = Zr, Ti, Co) for Permanent-Magnet Applications: Ab Initio Material Design Integrated with Experimental Characterization. *Phys. Rev. Appl.* **2020**, *13*, 064028. [CrossRef]
23. Landa, A.; Söderlind, P.; Moore, E.E.; Perron, A. Thermodynamics and Magnetism of $SmFe_{12}$ Compound Doped with Co and Ni: An Ab Initio Study. *Appl. Sci.* **2022**, *12*, 4860. [CrossRef]
24. Fukazawa, T.; Harashima, Y.; Miyake, T. First-principles study on the stability of $(R, Zr)(Fe, Co, Ti)_{12}$ against 2-17 and unary phases (R = Y, Nd, Sm). *Phys. Rev. Mater.* **2022**, *6*, 054404. [CrossRef]
25. Gabay, A.M.; Hadjipanayis, G.C. Mechanochemical synthesis of magnetically hard anisotropic RFe10Si2 powders with R representing combinations of Sm, Ce and Zr. *J. Magn. Magn. Mater.* **2017**, *422*, 43–48. [CrossRef]
26. Zhou, C.; Pinkerton, F.E. Magnetic hardening of $CeFe_{12-x}Mo_x$ and the effect of nitrogenation. *J. Alloys Compd.* **2013**, *583*, 345–350. [CrossRef]
27. Bhandari, C.; Paudyal, D. Enhancing stability and magnetism of $ThMn_{12}$-type cerium-iron intermetallics by site substitution. *Phys. Rev. Res.* **2022**, *4*, 023012. [CrossRef]
28. Snarski-Adamski, J.; Werwiński, M. Effect of transition metal doping on magnetic hardness of $CeFe_{12}$-based compounds. *J. Magn. Magn. Mater.* **2022**, *554*, 169309. [CrossRef]
29. Gabay, A.M.; Hadjipanayis, G.C. $ThMn_{12}$-type structure and uniaxial magnetic anisotropy in $ZrFe_{10}Si_2$ and $Zr_{1-x}Ce_xFe_{10}Si_2$ alloys. *J. Alloys Compd.* **2016**, *657*, 133–137. [CrossRef]
30. Barandiaran, J.M.; Martin-Cid, A.; Schönhöbel, A.M.; Garitaonandia, J.S.; Gjoka, M.; Niarchos, D.; Makridis, S.; Pasko, A.; Aubert, A.; Mazaleyrat, F.; et al. Nitrogenation and sintering of $(Nd\text{-}Zr)Fe_{10}Si_2$ tetragonal compounds for permanent magnets applications. *J. Alloys Compd.* **2019**, *784*, 996–1002. [CrossRef]
31. Gjoka, M.; Sarafidis, C.; Giannopoulos, G.; Niarchos, D.; Hadjipanayis, G.; Tabares, J.A.; Alcázar, G.A.P.; Zamora, L.E. Effect of cobalt substitution on structure and magnetic properties of $Nd_{0.4}Zr_{0.6}Fe_{10-x}Co_xSi_2$ (x = 0–3) alloys and their ribbons. *J. Rare Earths* **2019**, *37*, 1096–1101. [CrossRef]
32. Martin-Cid, A. Development of New High Anisotropy Phases for Permanent Magnet Applications. PhD Thesis, Universidad del Pais Vasco, Pais Vasco, Spain, 2018.
33. Kobayashi, K.; Furusawa, D.; Suzuki, S.; Kuno, T.; Urushibata, K.; Sakuma, N.; Yano, M.; Shoji, T.; Kato, A.; Manabe, A.; et al. High-Temperature Stability of $ThMn_{12}$ Magnet Materials. *Mater. Trans.* **2018**, *59*, 1845–1853. [CrossRef]
34. Lutterotti, L. Total pattern fitting for the combined size–strain–stress–texture determination in thin film diffraction. *Nucl. Instrum. Methods Phys. Res. Sect. B Beam Interact. Mater. Atoms* **2009**, *268*, 334–340. [CrossRef]
35. Gigla, M.; Pączkowski, P. *ElDyf for Windows*; Version 2.1; Institute of Materials Science, University of Silesia in Katowice: Katowice, Poland, 2005.
36. Kołodziej, M.; Śniadecki, Z. Thermodynamic Modeling of Formation Enthalpies of Amorphous and Crystalline Phases in Zr, Nd, and Ce Substituted Fe-Si System. *Appl. Sci.* **2023**, *13*, 1966. [CrossRef]
37. Randrianantoandro, N.; Gaffet, E.; Mira, J.; Greneche, J.-M. Magnetic hyperfine temperature dependence in Fe–Si crystalline alloys. *Solid State Commun.* **1999**, *111*, 323–327. [CrossRef]
38. Varga, L.K.; Mazaleyrat, F.; Kovac, J.; Greneche, J.M. Structural and magnetic properties of metastable $Fe_{1-x}Si_x$ ($0.15 < x < 0.34$) alloys prepared by a rapid-quenching technique. *J. Phys. Condens. Matter* **2002**, *14*, 1985–2000. [CrossRef]
39. Gjoka, M.; Psycharis, V.; Devlin, E.; Niarchos, D.; Hadjipanayis, G. Effect of Zr substitution on the structural and magnetic properties of the series $Nd_{1-x}Zr_xFe_{10}Si_2$ with the $ThMn_{12}$ type structure. *J. Alloys Compd.* **2016**, *687*, 240–245. [CrossRef]
40. Zhao, L.Z.; Yu, H.Y.; Guo, W.T.; Zhang, J.S.; Zhang, Z.Y.; Hussain, M.; Liu, Z.W.; Greneche, J.M. Phase and Hyperfine Structures of Melt-spun Nanocrystalline $(Ce_{1-x}Nd_x)_{16}Fe_{78}B_6$ Alloys. *IEEE Trans. Magn.* **2017**, *53*, 1–5. [CrossRef]
41. Zhao, L.; Li, C.; Hao, Z.; Liu, X.; Liao, X.; Zhang, J.; Su, K.; Li, L.; Yu, H.; Greneche, J.-M.; et al. Influences of element segregation on the magnetic properties in nanocrystalline Nd-Ce-Fe-B alloys. *Mater. Charact.* **2018**, *148*, 208–213. [CrossRef]
42. Idzikowski, B.; Wolf, M.; Handstein, A.; Nenkov, K.; Engelmann, H.J.; Stobiecki, F.; Muller, K.-H. Inverse giant magnetoresistance in granular Nd/sub 2/Fe/sub 14/B//spl alpha/-Fe. *IEEE Trans. Magn.* **1997**, *33*, 3559–3561. [CrossRef]